View Article Online
View Journal

Materials
Advances

Accepted Manuscript

This article can be cited before page numbers have been issued, to do this please use: T. Enkhbat, J. Park, S. H. Lee, S. Park and J. H. Jang, *Mater. Adv.*, 2026, DOI: 10.1039/D5MA01453K.

ROYAL SOCIETY
OF **CHEMISTRY**

rsc.li/materials-advances

View Article Online
DOI: 10.1039/D5MA01453K

Ga Back-Graded $CuInSe_2$ Thin Films for High-Performance Near-Infrared Photodetectors

Temujin Enkhbat[a], Jieun Park[a], Sang Hun Lee[b], Seong Ju Park[a], Jae Hyung Jang[a]*

[a]Department of Energy Engineering, KENTECH Institute of Energy Materials and Devices, Korea Institute of Energy Technology, Naju 58330, Republic of Korea

[b]School of Electrical Engineering and Computer Science, Gwangju Institute of Science and Technology, Gwangju 61005, Republic of Korea

Corresponding Author

* Jae Hyung Jang
E-mail: jjang@kentech.ac.kr

ABSTRACT:

Copper indium selenide ($CuInSe_2$, CISe) thin films are promising materials for optoelectronic applications due to their tunable bandgap, high absorption coefficient, and excellent thermal stability. In this work, the performance of CISe-based photodetectors is enhanced through controlled gallium (Ga) back-side incorporation, forming a compositional grading profile within the absorber layer. The Ga-induced grading improves film crystallinity and grain growth while suppressing recombination losses, leading to enhanced junction quality and carrier extraction. As a result, the optimized Ga-incorporated device exhibits a peak responsivity of 0.67 A W^{-1} and a specific detectivity (D^*) exceeding 10^{12} Jones under 1064 nm illumination. In addition, transient photoresponse measurements reveal a significant reduction in response time ($\tau_{10\%\text{-}90\%}$) from 0.48 ms to 0.18 ms, indicating accelerated carrier transport dynamics. Compared with undoped CISe devices, the Ga-graded photodetectors demonstrate improved external quantum efficiency (EQE), reduced series resistance (R□), and suppressed leakage pathways. These results highlight the effectiveness of Ga back grading in simultaneously optimizing both steady-state sensitivity and temporal response, establishing Ga-graded CISe thin films as promising and cost-effective candidates for high-performance near-infrared (NIR) photodetection and integrated optoelectronic applications.

KEYWORDS: Near-infrared photodetectors, $CuInSe_2$ (CISe), Ga back grading, thin-film photodetectors, spectral responsivity, specific detectivity, carrier dynamics.

View Article Online
DOI: 10.1039/D5MA01453K

1. Introduction

Near-infrared (NIR) photodetectors play a critical role in modern optoelectronic systems, supporting a wide range of applications including telecommunications, biomedical imaging, security surveillance and environmental monitoring.[1,2] As technology advances, the demand for high-performance, cost-effective, and environmentally sustainable NIR photodetectors continues to grow, driving extensive research into novel materials and device architectures.[3] Efficient NIR photodetection requires materials with strong NIR absorption, low dark current, effective charge separation, and high carrier mobility to ensure fast response and minimal energy loss.[4] Additional considerations such as scalability, integration compatibility, and long-term stability are essential for practical implementation.

Various semiconductor materials have been explored for NIR detection, each offering trade-offs in spectral range, performance, cost, and compatibility. Silicon (Si), the most established optoelectronic material, has a bandgap of 1.12 eV, limiting its NIR sensitivity to wavelengths below ~1100 nm.[5] While Si photodetectors, such as PIN diodes and avalanche photodiodes, benefit from mature CMOS fabrication and low cost, they fall short for longer-wavelength applications.[6] III–V semiconductors like InAs, GaAs, and InGaAs, with bandgaps around 0.72 eV, provide superior NIR performance up to 1700 nm and are widely used in fiber-optic communication and biomedical imaging.[7] However, their fabrication relies on costly epitaxial growth and often requires cooling to reduce dark current, posing integration and economic challenges.[8] Germanium (Ge), with a narrower bandgap of 0.67 eV, extends detection to ~1600 nm but suffers from high dark current and thermal instability unless passivated or cooled.[9] Emerging materials like organic semiconductors and quantum dots (e.g., PEDOT or PbS) provide tunable NIR absorption and low-cost fabrication on flexible substrates. However, their inefficient charge transport, environmental instability, and susceptibility to degradation from oxygen and moisture limit their long-term performance unless encapsulated or chemically modified.[10]

To address the limitations of conventional photodetector materials, researchers have increasingly explored chalcogenide semiconductors, which offer tunable optoelectronic properties

View Article Online
DOI: 10.1039/D5MA01453K

and scalability for near-infrared (NIR) photodetection.[11,12] Among these, copper indium gallium selenide (CIGSe) is a well-established material in thin-film photovoltaics, recognized for its high power conversion efficiency and a tunable bandgap of 1.1-1.5 eV.[13] In CIGSe, higher Ga content raises the open-circuit voltage but also widens the bandgap, limiting spectral response beyond ~1100 nm.[14] This constraint reduces their suitability for NIR photodetection, where longer-wavelength sensitivity is critical. In comparison, copper indium selenide (CISe), a closely related I–III–VI$_2$ chalcogenide, possesses a narrower and fixed bandgap of 1.0 eV, enabling more efficient absorption beyond 1100 nm.[15] CISe also exhibits strong optical absorption, high carrier mobility, and long carrier diffusion lengths, along with a scalable composition, making it an attractive and sustainable material for NIR photodetector applications.[16] Although CISe has primarily been studied in the context of photovoltaics, recent research highlights its promising potential for use in photodetector devices.[17,18]

In this study, we report a CISe-based thin-film photodetector in which device performance is enhanced through controlled Ga incorporation at the back side of the absorber, partially substituting the In^{3+} lattice sites. In contrast to conventional CIGSe solar cells, where strong Ga grading is typically employed to widen the bandgap and increase the open-circuit voltage, our approach introduces a moderate compositional gradient that preserves a relatively narrow bandgap near the front junction, thereby maintaining efficient NIR absorption. This tailored bandgap profile improves film crystallinity, promotes efficient carrier collection, and suppresses recombination losses while retaining strong long-wavelength sensitivity. Through comprehensive structural, electrical, and optoelectronic characterizations, we elucidate the relationship between Ga-induced compositional grading, junction properties, and photodetector performance. The optimized device exhibits a responsivity of 0.67 A W^{-1} at 1064 nm and a shot-noise-limited specific detectivity (D^*) on the order of 10^{12} Jones under zero-bias condition. These values fall within the same order of magnitude as steady-state detectivity reported for InGaAs and Ge photodetectors under similar shot-noise-limited assumptions. Collectively, these results demonstrate that Ga-graded CISe provides an effective strategy for simultaneously optimizing carrier extraction and NIR sensitivity,

View Article Online
DOI: 10.1039/D5MA01453K

establishing CISe as a promising and potentially cost-effective platform for multifunctional optoelectronic devices that combine photovoltaic energy conversion with high-sensitivity NIR photodetection.

2. Experimental

2.1. Device fabrication

Soda-lime glass (SLG) substrates coated with Mo (1.0 μm thickness) were cleaned to remove organic contaminants by ultrasonication in acetone for 5 minutes, followed by methanol for 5 minutes to remove residual acetone and additional contaminants. After cleaning, the SLG/Mo substrates were rinsed with deionized water (DIW) and dried using compressed nitrogen gas to prevent water spots and ensure a clean surface. The CISe layer was deposited via a three-stage co-evaporation process. In the first stage, In, Ga, and Se were co-evaporated for 6 minutes at a substrate temperature of 380 °C, with Ga co-deposition duration varied as 0 minutes (G0), 3 minutes (G3), and 6 minutes (G6) to produce pure CISe and Ga back-graded CISe profiles with increasing Ga concentration toward the back contact. In the second stage, Cu and Se were evaporated for 11 minutes at 580 °C. The third stage involved co-deposition of In and Se for 20 minutes at 580 °C. Finally, the deposited films were cooled under a Se flux until the substrate temperature reached 350 °C.

A 60-nm-thick CdS buffer layer was deposited onto the CISe absorber via chemical bath deposition (CBD) without any pre-treatment, following the procedure described in our previous report.[19] After deposition, the samples were rinsed with deionized water and air-annealed at 250 °C for 10 minutes to improve CdS adhesion. A transparent conductive oxide (TCO) top contact was then formed by sequentially depositing a 60-nm-thick intrinsic zinc oxide (i-ZnO) layer and a 300-nm-thick indium tin oxide (ITO) layer using a 3-inch radio-frequency magnetron sputtering system. Finally, a 100-nm-thick silver (Ag) front electrode was deposited by electron-beam evaporation. All CISe photodetector devices (G0, G3, and G6) were fabricated with identical structures, maintaining a total device area of 9 mm² and an optical window of 3.2 mm² to ensure consistent performance comparisons.

View Article Online
DOI: 10.1039/D5MA01453K

2.2. Device measurements

The surface morphology and cross-sectional chemical composition of the CISe (G0, G3, and G6) films were examined using field-emission scanning electron microscopy (FESEM, SU8600, Hitachi) equipped with energy-dispersive X-ray spectroscopy (EDS). The crystal structure was analyzed by X-ray diffraction (XRD, SmartLab 9 kW, Rigaku). Current density–voltage (J–V) characteristics were measured under AM 1.5G illumination (100 mW cm^{-2}) using a solar simulator (Oriel Sol3A Class AAA, Newport Corporation). External quantum efficiency (EQE) was evaluated using a QUANTX-300 system. Near-infrared (NIR) absorption spectra were recorded with a UV–Vis–NIR spectrometer (Cary 5000, Agilent Technologies). Photodetection measurements were performed using a 1064 nm laser diode as the illumination source. The incident optical power was measured at the device-plane using a calibrated optical power sensor (J-10MB-LE, Coherent) under identical alignment conditions. The laser spot diameter, defined as the $1/e^2$ width of the near-Gaussian beam profile delivered through the optical fiber, was estimated to be ~0.9 mm. This spot size is smaller than the active device diameter (2 mm), ensuring that the illuminated region was fully contained within the device's optical window (~3.2 mm^2) during measurements. Consequently, responsivity was calculated based on the total incident optical power on the device. Beam alignment was optimized using a precision XYZ translation stage to center the Gaussian peak on the device active area. The Ag top electrode geometry (Fig. S1) was kept identical across all devices to ensure consistent comparative analysis. Transient photoresponse measurements were conducted under square laser square modulated by using a function generator (Agilent 33220A). The temporal photocurrent response was monitored using a digital oscilloscope (Tektronix DPO 7254). Capacitance–voltage (C–V) measurements were carried out using a precision LCR meter (Agilent E4980A) at a frequency of 1 kHz to evaluate the junction capacitance and built-in potential through Mott–Schottky analysis. Dark and photo-generated current–voltage characteristics were recorded using a semiconductor parameter analyzer (Keithley 2450 SourceMeter).

View Article Online
DOI: 10.1039/D5MA01453K

3. Results and discussion

3.1. Characteristics of CISe films

Fig. 1a–f and Fig. S2 present the field-emission scanning electron microscopy (FESEM) images and X-ray diffraction (XRD) results for pristine CISe (G0) and Ga-incorporated CISe samples (G3 and G6, corresponding to Ga back-deposition durations of 3 and 6 minutes, respectively). The top-view FESEM images (Fig. 1a–c) reveal distinct differences in grain morphology and size evolution with Ga addition. The G0 sample exhibits a compact, polycrystalline microstructure with smaller, irregularly shaped grains. In contrast, the G3 sample shows a more defined, faceted grain structure with increased grain size, while the G6 sample continues the trend, displaying slightly larger grains than G3, with greater uniformity and reduced porosity.

The XRD patterns (Fig. S2) for the G0, G3, and G6 samples exhibit three main CISe-related peaks corresponding to the (112), (220)/(204), and (312)/(116) crystal planes, confirming the chalcopyrite crystal structure.[20] The dominant peaks shift slightly to higher 2θ angles with Ga addition due to lattice contraction induced by the substitution of smaller Ga^{3+} ions (ionic radius ~47 Å) for In^{3+} ions (ionic radius ~62 Å) in the CISe lattice, reducing the interplanar spacing (d) and increasing 2θ according to Bragg's law ($2d\sin\theta = n\lambda$).[21,22] Specifically, as shown in Table S4, the (112) peak shifts from 26.67° in G0 to 26.78° in G6, with a similar trend observed for the (220)/(204) and (312)/(116) peaks. In addition, the full width at half maximum (FWHM) values of the diffraction peaks decrease progressively from G0 to G6. The G0 sample exhibits the broadest peaks, indicating smaller and more disordered crystallites, while G6 shows the narrowest peaks, reflecting improved crystallinity and larger grain size. This trend is consistent with the FESEM observations and further supports the conclusion that Ga incorporation enhances structural ordering and promotes grain growth in CISe thin films.

To further examine the Ga distribution within the absorber layers, point energy-dispersive spectroscopy (EDS) measurements were performed at five positions from the bottom (P1) to the

View Article Online
DOI: 10.1039/D5MA01453K

top surface (P5) of the G0, G3, and G6 samples. The corresponding cross-sectional FESEM images (Fig. 1d–f) reveal detailed film morphologies and thicknesses of 1.84, 1.89 and 1.91 μm for G0, G3, and G6, respectively. The slight increase in thickness for the Ga-incorporated samples (G3 and G6) is attributed to the Ga back-deposition process, which promotes material accumulation during co-evaporation. In addition to increasing film thickness, the presence of Ga appears to facilitate grain growth and reduce intergranular voids, as indicated by the denser and more compact microstructures observed in the cross-sectional images.

Fig. 1g–i and Table S3 show the detailed EDS results of the CISe absorber films. In the Ga-free G0 sample, Cu and In concentrations remain nearly constant across all measured points, indicating a uniform distribution in the absence of Ga. In contrast, the G3 and G6 samples exhibit a clear compositional gradient, with Ga concentrations vary from 2.17 at.% (P1) to 0.11 at.% (P5) in G3, and from 4.13 at.% to 0.37 at.% in G6. As the Ga content decreases from P1 to P5, a corresponding increase in both Cu and In contents is observed in the G3 and G6 samples. This behavior aligns with the well-established In–Ga lattice substitution mechanism and the Cu–Ga anti-correlation, commonly reported in chalcopyrite absorbers.[23] In Ga-rich regions near the back contact, Ga preferentially replaces In on group-III lattice sites while simultaneously suppressing Cu incorporation, due to both the lower chemical activity of Cu and the reduced number of energetically favorable Cu lattice sites in Ga-rich local environments.[24] Consequently, as the Ga concentration declines toward the front surface, the lattice becomes more permissive to Cu and In uptake, resulting in the observed Cu-rich and In-rich surface composition.

3.2. Characterization of CISe devices

Fig. 2 illustrates the CISe photodetector architecture and its corresponding energy band alignment. As shown in Fig. 2a, the device consists of a Mo back contact deposited on soda-lime glass (SLG), followed by the CISe absorber, CdS buffer layer, ZnO/ITO window layers and a patterned Ag top contact. This stacked structure allows illumination through the transparent ZnO/ITO layers, with photogenerated carriers collected primarily via the Mo back contact. The

View Article Online
DOI: 10.1039/D5MA01453K

energy band diagram in Fig. 2b depicts the relative conduction and valence band levels across the layers, revealing a favorable alignment for efficient charge separation and transport. Notably, the CISe/CdS interface exhibits a modest conduction band offset (spike-like), which promotes electron extraction toward the front contact while minimizing interfacial recombination. The wider bandgaps of ZnO and ITO ensure high transparency in the near-infrared region, whereas the Ga-graded CISe absorber provides efficient NIR absorption and improved internal electric fields.

To further assess the electrical and optical performance of the CISe devices, we analyzed the photovoltaic characteristics as shown in Fig. 3a and Table 1. The Ga-free G0 device exhibits a photovoltaic power conversion efficiency (PCE) = 2.33%, open-circuit voltage (V_{oc}) = 258 mV, short-circuit current density (J_{sc}) = 29.1 mA cm^{-2}, fill factor (FF) = 30.6%, series resistance (R_s) = 32.6 Ω, and shunt resistance (R_{sh}) = 74 Ω. The G3 device shows moderate improvement, with PCE = 3.31%, V_{oc} = 284 mV, J_{sc} = 30.8 mA cm^{-2}, FF = 34.4%, R_s = 28.2 Ω, and R_{sh} = 116 Ω. The G6 device demonstrates the highest performance, achieving PCE = 6.17%, V_{oc} = 330 mV, J_{sc} = 34.1 mA cm^{-2}, FF = 54.8%, R_s = 14.8 Ω, and R_{sh} = 720 Ω. Although the measured PCEs (2.33% for G0, 3.31% for G3, and 6.17% for G6) are lower than state-of-the-art CISe/CIGS solar cells (Table S1), this is expected because the present devices are optimized for NIR photodetection rather than for maximum photovoltaic efficiency. High-efficiency CISe/CIGS solar cells typically employ Ag alloying and optimized In/Ga supply sequences to facilitate large grain growth and suppress defect formation, thereby maximizing the V_{oc} and FF.[25,26] In contrast, the reversed Ga supply sequence adopted here preserves the desired back-grading profile to enhance 1064 nm responsivity but leads to higher defect density and increased recombination, thereby limiting V_{oc} and PCE. Nevertheless, this structural configuration improves NIR-specific performance metrics, yielding a responsivity of 0.67 A W^{-1} and a detectivity exceeding 10^{12} Jones under reverse bias. Similar trade-offs between photovoltaic efficiency and NIR photodetection performance have been reported in dual-function PV–PD devices.[27]

Fig. 3b and Fig. S3 present the EQE spectra and the extracted optical bandgaps (E_g). A slight blue shift in the EQE onset is observed for G3 and G6, consistent with the E_g increase from

View Article Online
DOI: 10.1039/D5MA01453K

0.99 eV (G0) to 1.01 eV (G3) and 1.02 eV (G6). To verify this trend, we additionally measured the NIR absorbance of G0, G3, and G6 films deposited on bare SLG and extracted their bandgaps using Tauc plots (Fig. S4). The Tauc-derived E_g values show the same progression as those obtained from the EQE analysis, confirming the consistency of the optical characterization. Moreover, this modest bandgap widening caused by Ga incorporation contributes to the enhanced V_{oc} and supports the reduction in bulk and interface recombination. Despite the small increase in E_g, the back-graded Ga profile allows G3 and G6 to maintain strong long-wavelength collection at 1064 nm, which is essential for NIR photodetection. To verify the consistency between the J–V and EQE measurements, the short-circuit current density was independently calculated from the EQE spectra using:

$$J_{sc,EQE} = q\int EQE(\lambda)\Phi_{AM1.5G}(\lambda)d(\lambda) \tag{1}$$

where q is the elementary charge and $\Phi_{AM1.5G(\lambda)}$ is the AM1.5G photon flux spectrum. The integrated current densities were 29.70, 31.36 and 34.53 mA cm^{-2} for the G0, G3, and G6 devices, respectively. These values fairly well match with the measured J–V results and reveal a systematic enhancement in photoresponse with increasing Ga content.

To further evaluate the spectral responsivity (R) in the NIR region, the EQE values of the G0, G3, and G6 devices were examined at 1064 nm. The G6 device exhibited the highest EQE of 78%, significantly outperforming G3 (65%) and G0 (59%) at this wavelength. EQE values directly relate to the R with following equation:

$$R = EQE\,\frac{q\lambda}{hc} \tag{2}$$

where, q is the elementary charge, λ is the incident wavelength, h is Planck's constant, c is the speed of light.[28] The calculated R values were 0.50, 0.56 and 0.67 A/W for G0, G3, and G6 devices, respectively. These results confirm that Ga incorporation not only improves the structural quality of CISe films but also significantly enhances their optoelectronic performance, particularly for NIR photodetection applications.

View Article Online
DOI: 10.1039/D5MA01453K

3.3. Characterization of CISe photodetectors

To investigate the photo-response behavior of G0, G3, and G6 devices, their reverse-bias I–V characteristics were measured under 1064 nm laser illumination with optical power levels ranging from 0 to 4 mW, as shown in Fig. 4a–c. All devices exhibit increasing photocurrent with rising light intensity, but the magnitude of enhancement differs significantly among the samples. The G0 device (Fig. 4a) shows only modest separation between dark and illuminated currents, accompanied by a relatively high dark current and a pronounced positive slope under reverse bias. The elevated dark current in the Ga-free device is associated with leakage pathways and defect-assisted generation–recombination (G–R) processes within the absorber layer.[29] This interpretation is supported by the low shunt resistance (R_{sh}) and reduced open-circuit voltage (V_{oc}) observed in the photovoltaic measurements. The G3 device (Fig. 4b) exhibits improved separation between dark and illuminated currents compared to G0, indicating enhanced photoresponse. However, a noticeable positive slope and a relatively large dark current (~1 mA) remain under reverse bias, suggesting that limited Ga incorporation is insufficient to fully suppress back-contact leakage and defect-mediated recombination pathways. In contrast, the G6 device (Fig. 4c) demonstrates the largest separation between dark and illuminated currents across the entire optical power range, together with a substantially reduced dark current. The reverse-bias curves exhibit a near-zero slope, indicating high shunt resistance and suppressed leakage current. This behavior suggests improved back-contact band alignment and reduced defect-assisted recombination with optimized Ga incorporation. The reduced leakage enables efficient carrier collection under reverse bias and results in rapid photocurrent saturation, rendering the photocurrent largely independent of applied voltage.[30]

The photodetection performance of the CISe devices was evaluated under steady-state 1064 nm illumination at zero bias (0 V) and compared with state-of-the-art NIR photodetectors (Table S2). As shown in Fig. S5, the G0, G3, and G6 devices exhibit *R* values of 0.51, 0.54 and 0.67 A W^{-1}, under 1 mW incident optical power. A clear and systematic enhancement in *R* is

View Article Online
DOI: 10.1039/D5MA01453K

observed with increasing Ga incorporation, with the G6 device demonstrating the highest photoresponse. To assess the stability and linearity of the photodetection behavior, measurements were also conducted under higher illumination intensities of 2, 3, and 4 mW. The average R values across these power levels remain consistent and show good agreement with the responsivity derived from the EQE spectra at 1064 nm, confirming the reliability of the measurement and the absence of significant power-dependent saturation effects. The near-linear photocurrent response with increasing optical power further indicates efficient carrier generation and extraction without substantial recombination-induced losses under the tested conditions.

Fig. 5a illustrates the dark current density as a function of applied voltage for the G0, G3, and G6 devices. At +1.0V forward bias, the dark current densities rise from 3.01×10^{-2} (G0) to 6.98×10^{-2} (G3) and 1.21×10^{-1} A cm^{-2} (G6), whereas at -0.3V reverse bias, they drop progressively to 1.26×10^{-3} (G0), 4.98×10^{-4} (G3) and 3.83×10^{-4} A cm^{-2} (G6), respectively. This opposite polarity-dependent ordering reflects the asymmetric carrier transport induced by Ga back-grading. Under forward bias, carrier injection is dominated by the CdS/CISe front junction and the reduced interface recombination in G6 lowers the injection barrier, resulting the highest forward current and improved diode characteristics.[31] Under reverse bias, leakage at the CISe/Mo back contact limits the current and the Ga-rich region in G6 introduces a pronounced conduction-band spike that effectively suppresses these leakage pathways. As a result, G6 exhibits the lowest reverse dark current and reduced Shot noise.[32]

The specific detectivity ($D*$) of the devices was calculated using the shot-noise-limited expression:

$$D^* = \frac{R\sqrt{A}}{\sqrt{2q\,J_{dark}}} \tag{3}$$

where R is the responsivity, A is the effective device area, q is the elementary charge, and J_{dark} is the dark current density.[33] This expression assumes that the dominant noise source in the device

View Article Online
DOI: 10.1039/D5MA01453K

originates from the shot noise associated with the dark current. Under this assumption, the noise current (I_N) can be expressed as:

$$I_N = \sqrt{2qI_{dark}\Delta f} \tag{4}$$

where I_{dark} is the dark current and Δf is the electrical bandwidth (taken as 1 Hz). It should be noted that this calculation represents an ideal detectivity estimated under the shot-noise limit, and additional noise contributions such as (1/f) noise, generation–recombination noise, or contact-induced excess noise were not explicitly evaluated in this study.

To provide a comprehensive assessment of device performance, the specific detectivity (*D**) was evaluated under both zero-bias and a reverse bias of -0.3 V, allowing for a comparison between self-powered potential and active operating characteristics. Under zero-bias conditions, the photodetectors operate in a photovoltaic mode where the built-in electric field is sufficient to separate photogenerated electron–hole pairs, resulting in dark current densities of 2.59×10^{-7}, 5.61×10^{-8}, and 7.08×10^{-9} A cm^{-2} and *D** values of 3.17×10^{11}, 7.26×10^{11}, and 2.51×10^{12} Jones for G0, G3, G6, respectively.[34] In contrast, evaluating the devices under a reverse bias of -0.3 V represents a more conservative estimate of performance during practical operation. At this bias, the *D** values were determined to be 1.44×10^{9}, 2.41×10^{9}, and 3.42×10^{9} Jones for the corresponding samples. While the detectivity at -0.3 V reflects the expected increase in dark current under an external field, the G6 device maintains the highest biased *D**, demonstrating that Ga-grading effectively suppresses leakage pathways even under active operating conditions. Ultimately, this dual-condition analysis highlights the synergistic balance between the intrinsic self-powered capability of the heterojunction and its structural robustness under an external field.

Fig. 5b presents the spectral detectivity of the G0, G3, and G6 devices as a function of wavelength. The G0 device exhibits the lowest detectivity across the measured spectrum, generally remaining within the 10^{10}~10^{11} Jones range. While G3 device shows a notable improvement over G0, the G6 device demonstrates a superior *D** exceeding 10^{12} Jones in the NIR region. This enhancement can be attributed to the synergistic effect of increased responsivity and the

View Article Online
DOI: 10.1039/D5MA01453K

significantly suppressed dark current density achieved through Ga-grading. These results highlight the effectiveness of Ga-incorporation in CISe-based photodetectors, with the G6 device demonstrating a well-optimized architecture for high-sensitivity NIR applications.

To evaluate the dynamic performance of the devices, transient photocurrent measurements were conducted under square modulated laser illumination, as shown in Fig. 5c. The response speed was quantified by extracting the rise time ($\tau_{10\%\text{-}90\%}$), which was determined to be 0.48 ms, 0.23 ms, and 0.18 ms for G0, G3, and G6, respectively (Table 2). The progressive reduction in response time with increasing Ga incorporation indicates more efficient carrier generation and extraction dynamics within the graded CISe absorber. To further elucidate the physical origin of this improvement, capacitance–voltage (C–V) measurements were analyzed using Mott–Schottky plots ($1/C^2$ vs. V), as presented in Fig. S6. The extracted built-in potentials (V_{bi}) increased from 362 mV (G0) to 480 mV (G3) and 561 mV (G6), while the junction capacitance (C) at 0 V and 1 kHz decreased from 25.4 nF (G0) to 20.6 nF (G6). The simultaneous increase in V_{bi} and reduction in C indicate a widening of the depletion region and a strengthened internal electric field.[35] Such an enhanced field facilitates more efficient separation and drift-assisted transport of photogenerated carriers while suppressing recombination losses within the absorber layer. Furthermore, the reduced junction capacitance lowers the capacitive component of the device impedance, leading to a smaller RC time constant and consequently a faster electrical response.[36] As a result, the G6 device exhibits the fastest transient behavior among the investigated samples, with the photocurrent demonstrating a significantly reduced rise time. These results confirm that Ga-induced compositional grading strengthens the junction electric field and accelerates carrier extraction, thereby enabling improved temporal response and high-performance NIR photodetection.

4. Conclusions

This study demonstrates the development of Ga-graded CISe thin-film devices for high-performance NIR photodetection. Controlled Ga incorporation at the back of the absorber establishes a compositional grading profile that improves film quality and junction characteristics

View Article Online
DOI: 10.1039/D5MA01453K

while preserving a relatively narrow bandgap near the front junction for efficient NIR absorption. Among the investigated devices, the G6 sample exhibits the best overall performance, delivering a responsivity of 0.67 A W^{-1} at 1064 nm and a shot-noise-limited detectivity of 2.51×10^{12} Jones under zero-bias operation. Transient measurements confirm a clear enhancement in device speed, with the rise time ($\tau_{10\%\text{-}90\%}$) improving from 0.48 ms (G0) to 0.18 ms (G6), while capacitance–voltage analysis shows consistent trends indicative of improved junction properties. Although the detectivity values are derived under shot-noise-limited, steady-state conditions, they remain comparable in order of magnitude to those reported for InGaAs and Ge photodetectors under similar assumptions. Notably, even the undoped G0 device exhibits measurable NIR responsivity, highlighting the intrinsic photodetection capability of CISe absorbers. Overall, these results demonstrate that Ga-induced bandgap grading effectively enhances both steady-state and dynamic device characteristics, establishing Ga-graded CISe as a promising and potentially cost-effective platform for NIR photodetectors and multifunctional optoelectronic applications.

Author contributions

Jae Hyung Jang conceived, conceptualized, designed and supervised the overall project. Temujin Enkhbat investigated, performed the experiments and wrote the draft. Jieun Park, Sang Hun Lee and Seongju Park provided technical support for the project. All the authors discussed the results and commented on the manuscript.

Conflicts of interest

The authors declare no competing financial interest.

Acknowledgement

This work was supported by the Regional Innovation Mega Project program (2023-DD-UP-0015) through the Korea Innovation Foundation funded by the Ministry of Science and ICT. Additionally, this study is part of the research project (R23XH02) funded by the Open R&D program of Korea Electric Power Corporation.

View Article Online
DOI: 10.1039/D5MA01453K

References

1. Q. Li, Y. Guo, Y. Liu, Chem. Mater., 2019, 31, 6359-6379.
2. K. Gundepudi, P. M. Neelamraju, S. Sangaraju, G. K. Dalapati, W. B. Ball, S. Ghosh, S. Chakrabortty, J. Mater. Sci., 2023, 58, 13889-13924.
3. Q. Wang, Y. Zhang, Z. Wei, Chin. J. Chem., 2023, 41, 958-978.
4. N. Ding, Y. Wu, W. Xu, J. Lyu, Y. Wang, L. Zi, L. Shao, R. Sun, N. Wang, S. Liu, Light Sci. Appl., 2022, 11, 91.
5. Y. Berencén, S. Prucnal, F. Liu, I. Skorupa, R. Hübner, L. Rebohle, S. Zhou, H. Schneider, M. Helm, W. Skorupa, Sci. Rep., 2017, 7, 43688.
6. J. Liu, S. Cristoloveanu, J. Wan, Phys. Status Solidi A, 2021, 218, 2000751.
7. B. Guo, B. Liang, J. Zheng, S. Ahmed, S. Krishna, A. Ghosh, J. Campbell, ACS Photonics, 2024, 11, 1419.
8. Y. Liang, C. P. P. Veeramalai, G. Lin, X. Su, X. Zhang, S. Feng, Y. Xu, C. Li, Nanotechnology, 2022, 33, 222003.
9. G. Yang, J. Li, M. Wu, X. Yu, J. Yu, Adv. Electron. Mater., 2023, 9, 2300340.
10. H. Ren, J.-D. Chen, Y.-Q. Li, J.-X. Tang, Adv. Sci., 2021, 8, 2002418.
11. J. Wang, Q. Pan, H. Xie, Y. Ma, M. Su, B. Chen, H. Wang, T. Xue, Z. Zhang, J. Chi, S. Li, Y. Song, Adv. Opt. Mater., 2022, 10, 2200173.
12. Y. Xu, R. Li, S. Bai, Y. Li, Z. Jia, Y. Yang, E. Cui, F. Yao, D. Wang, C. Lei, Q. Lin, Adv. Funct. Mater., 2023, 33, 2212523.
13. G. Regmi, A. Ashok, P. Chawla, P. Semalti, S. Velumani, S. N. Sharma, H. Castaneda, J. Mater. Sci. Mater. Electron., 2020, 31, 7286-7314.
14. J. Keller, K. Kiselman, O. Donzel-Gargand, N. M. Martin, M. Babucci, O. Lundberg, E. Wallin, L. Stolt, M. Edoff, Nat. Energy, 2024, 9, 467-478.
15. T. Maeda, W. Gong, T. Wada, Jpn. J. Appl. Phys., 2016, 55, 04ES15.
16. B. M. Palve, C. V. Jagtap, V. S. Kadam, C. D. Lokhande, H. M. Pathan, Engineered Sci., 2020, 12, 52-78.
17. S. T. Kim, J. S. Yoo, M. W. Lee, J. W. Jung, J.-H. Jang, Appl. Sci., 2021, 12, 2-7.
18. S. Li, J. H. Jang, W. Chung, H. Seung, S. I. Park, H. Ma, W. J. Pyo, C. Choi, D. S. Chung, D.-H. Kim, M. K. Choi, J. Yang, ACS Nano, 2023, 17, 20013-20023.

View Article Online
DOI: 10.1039/D5MA01453K

19. T. Enkhbat, S. T. Kim, J. Kim, J. H. Yun, S. J. Park, J.-H. Jang, ACS Appl. Energy Mater., 2025, 8, 134-140.
20. O. Volobujeva, J. Kois, K. Traksmaa, K. Muska, V. Bereznev, M. Grossberg, E. Mellikov, Thin Solid Films, 2008, 516, 7105-7109.
21. R. D. Shannon, Acta Crystallogr., Sect. A, 1976, 32, 751-767.
22. S. Fatimah, R. Ragadhita, D. F. AlHusaeni, A. B. D. Nandiyanto, ASEAN J. Sci. Eng., 2022, 2, 65-76.
23. Ishizuka, S.; Nishinaga, J.; Beppu, K.; Maeda, T.; Aoyagi, F.; Wada, T.; Yamada, A.; Chantana, J.; Nishimura, T.; Minemoto, T.; Islam, M. M.; Sakurai, T.; Terada, N., Phys. Chem. Chem. Phys., 2022, 24, 1262–1273.
24. S. M. Schleussner, T. Törndahl, M. Linnarsson, U. Zimmermann, T. Wätjen, M. Edoff, Prog. Photovolt: Res. Appl., 2012, 20, 284-293.
25. J. Keller, K. Kiselman, O. Donzel-Gargand, N. M. Martin, M. Babucci, O. Lundberg, E. Wallin, L. Stolt and M. Edoff, Nat. Energy, 2024, 9, 467–478.
26. M. Krause, S.-C. Yang, S. Moser, S. Nishiwaki, A. N. Tiwari and R. Carron, Sol. RRL, 2023, 7, 2201122.
27. X. Zeng, J. Lontchi, M. Zhukova, P. Bolt, M. Smor, L. Fourdrinier, G. Li and D. Flandre, Opt. Express, 2022, 30, 13875–13889.
28. F. Wang, X. Zou, M. Xu, H. Wang, H. Wang, H. Guo, J. Guo, P. Wang, M. Peng, Z. Wang, Adv. Sci., 2021, 8, 2100569.
29. G. Birant, J. de Wild, M. Meuris, J. Poortmans and B. Vermang, Appl. Sci., 2019, 9, 677.
30. A. V. Shevlyagin, D. L. Goroshko, E. A. Chusovitin, K. N. Galkin, N. G. Galkin, A. K. Gutakovskii, Sci. Rep., 2015, 5, 14795.
31. S. K. Cheung, N. W. Cheung, Appl. Phys. Lett., 1986, 49, 85-87.
32. J. Kublitski, A. Hofacker, B. K. Boroujeni, J. Benduhn, V. C. Nikolis, C. Kaiser, D. Spoltore, H. Kleemann, A. Fischer, F. Ellinger, Nat. Commun., 2021, 12, 551.
33. C. H. Ji, K. T. Kim, S. Y. Oh, RSC Adv., 2018, 8, 8302-8309.
34. J. Seo, Y. J. Kim and H. Yoo, Micromachines, 2022, 13, 2089.
35. J. T. Heath, J. D. Cohen and W. N. Shafarman, J. Appl. Phys., 2004, 95, 1000–1010.
36. X. Gong, M. Tong, Y. Xia, W. Cai, J. S. Moon, Y. Cao, G. Yu and A. J. Heeger, *Science*, 2009, **325**, 1665.

View Article Online
DOI: 10.1039/D5MA01453K

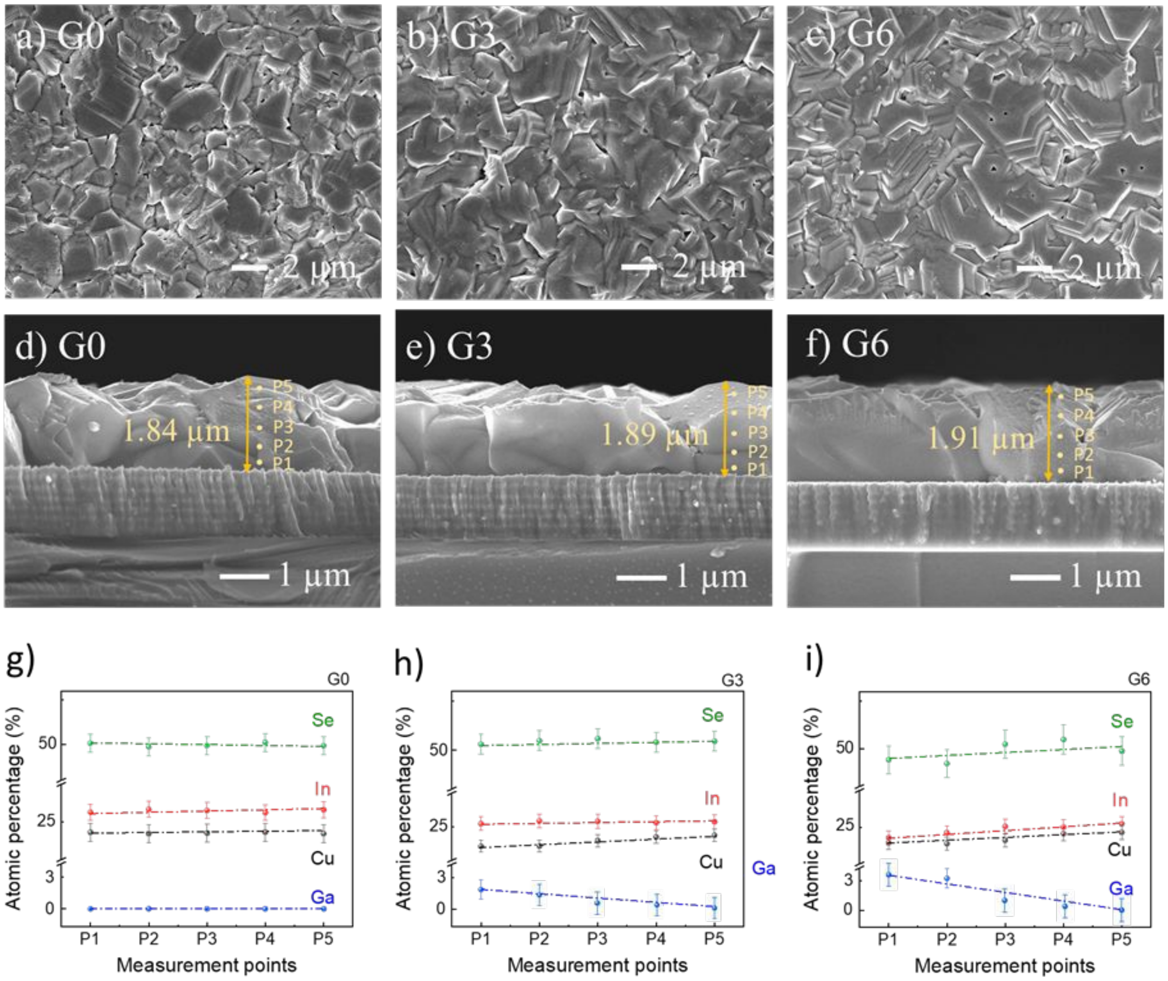

Fig. 1 FESEM characterization of CISe thin films. (a–c) Top-view and (d–f) Cross-sectional images of G0, G3, and G6 samples; (g–i) Point EDS analysis of G0, G3, and G6 samples.

View Article Online
DOI: 10.1039/D5MA01453K

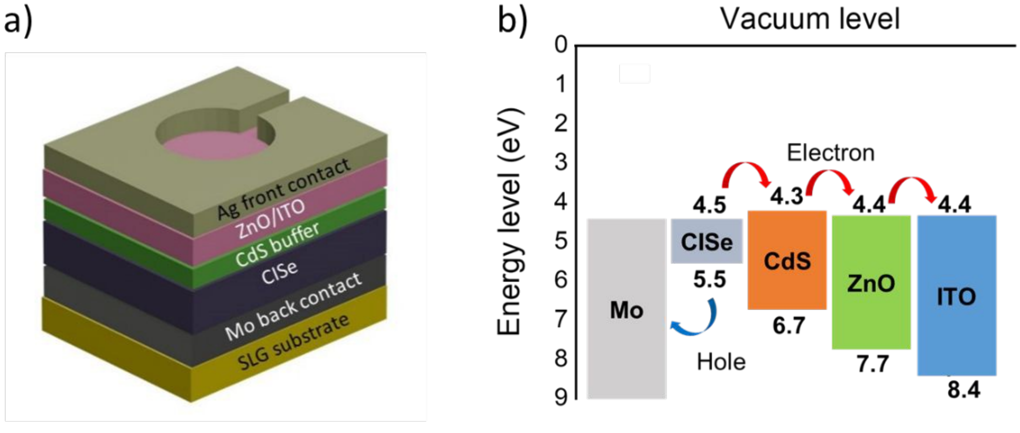

Fig. 2 Schematic illustration of CISe photodetector. (a) Device architecture and (b) corresponding band structure diagram.

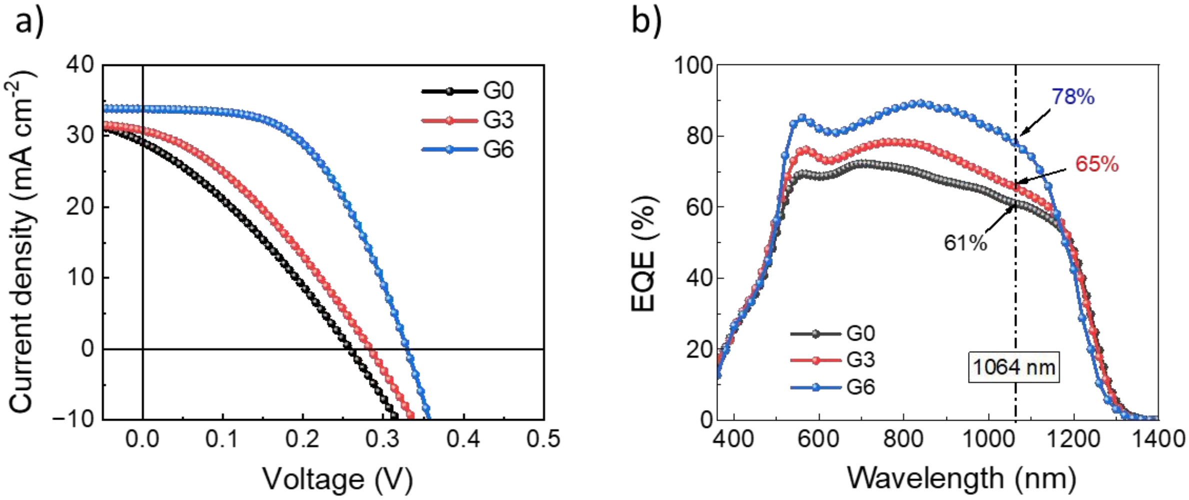

Fig. 3 Opto-electric performances of CISe devices. a) J-V and b) EQE curves of G0, G3 and G6 devices.

View Article Online
DOI: 10.1039/D5MA01453K

Table 1 Detailed performance parameters of CISe devices.

Device	Eff [%]	V_{oc} [mV]	J_{sc} [mA cm^{-2}]	FF [%]	R_s [Ω]	R_{sh} [Ω]	E_g [eV]	EQE at 1064 nm [%]	Responsivity [A W^{-1}]
G0	2.33	258	29.1	30.6	32.6	74.0	0.99	61	0.52
G3	3.31	284	30.8	34.4	28.2	116.1	1.01	65	0.56
G6	6.17	330	34.1	54.8	14.8	720.3	1.02	78	0.67

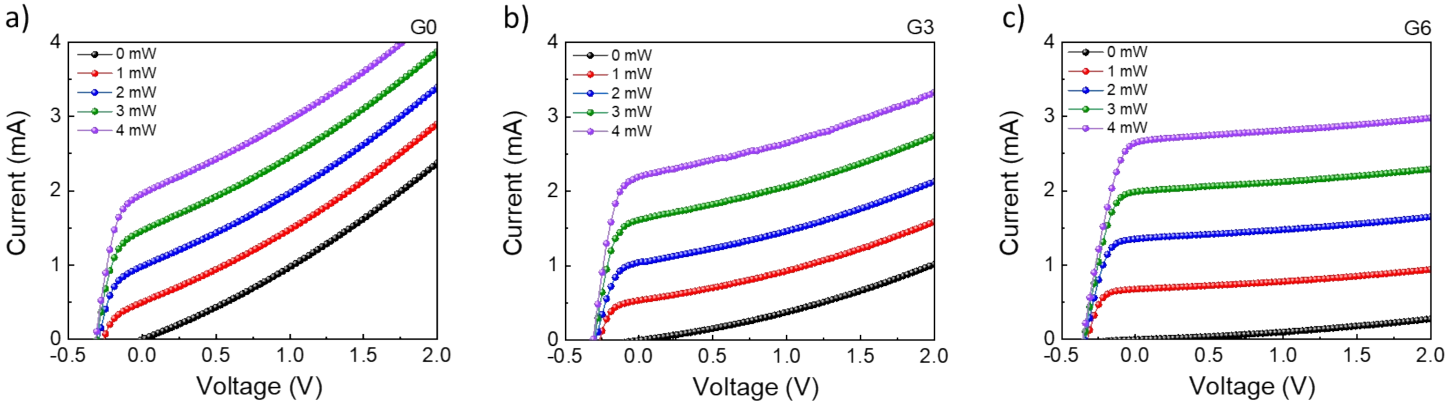

Fig. 4 Reverse bias I–V characteristics of CISe photodetectors. a) G0, b) G3 and c) G6 devices under illumination of 1064 nm.

View Article Online
DOI: 10.1039/D5MA01453K

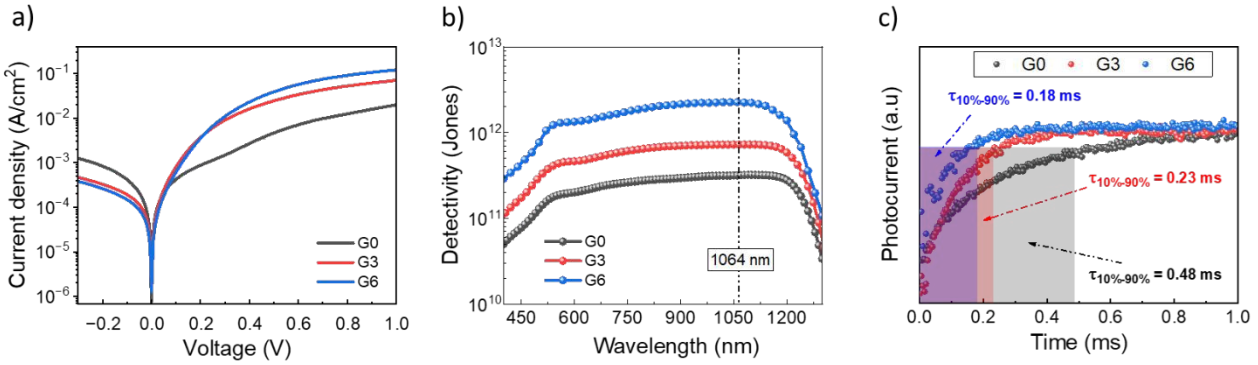

Fig. 5 Optoelectronic performance of the CISe photodetectors. a) Dark J-V characteristics, b) Spectral specific detectivity profiles as a function of wavelength, and c) Time-resolved photocurrent responses for G0, G3 and G6 devices.

Table 2 Electrical and transient photoresponse parameters of the CISe photodetectors.

Device	$1/C^2$ (0 V, 1KHz) [F^{-2}]	C [nF]	V_{bi} [mV]	Response time [ms]
G0	1.55×10^{15}	25.4	362	0.48
G3	2.14×10^{15}	21.6	480	0.23
G6	2.36×10^{15}	20.6	561	0.18

View Article Online
DOI: 10.1039/D5MA01453K

Data availability statement

The data that support the findings of this study are available from the corresponding author upon reasonable request.

Supplementary information (SI): A schematic layout of the Ag top electrode, State-of-the-art CISe and CIGS solar cells and NIR photodetectors, FESEM–EDS elemental analysis, XRD spectra with FWHM analysis, Optical bandgap and NIR absorption spectra, Photo-current dependency on illumination power, Mott-Schottky plots.